

Response of Plasma Density and Radiation to TESPEL Ablation in LHD

SERGEEV Vladimir Yu., TAMURA Naoki¹, KOSTRIOUKOV Artem Yu.², INAGAKI Shigeru²,
KHLOPENKOV Konstantin V.², KAWAHATA Kazuo², NAGAYAMA Yoshio²,
NARIHARA Kazumichi², PETERSON Byron J.², TANAKA Kenji², TOKUZAWA Tokihiko²,
SUDO Shigeru² and the LHD Experimental Group²

State Technical University, Polytechnicheskaya 29, St. Petersburg, 195251, Russia

¹ *National Institute for Fusion Science, Toki 509-5292, Japan*

² *Graduate University for Advanced Studies, Hayama 240-0193, Japan*

(Received: 11 December 2001 / Accepted: 25 June 2002)

Abstract

Perturbations of electron density and total plasma radiation profiles were measured and simulated in cases of both pure polystyrene shell and shell with Ti tracer (TESPEL) pellet injections into LHD plasmas. After establishing an ionization balance up to Li-like impurity ions of the ablated material, a good agreement between measured and simulated profiles was obtained taking into account pellet deposition measured by ablation light with ± 3 cm accuracy and using “average ion” dependencies of both the impurity charge state $\langle Z(T_e) \rangle$ and radiative rate $\langle Q_{\text{rad}}(T_e) \rangle$. No significant drift of the ablated material was observed since the agreement was sensitive to the pellet deposition profile.

Keywords:

pellet injection, ablation, density deposition, radiation

1. Introduction

The convenient, “average ion” model for calculations of the charge state and loss rate radiation of impurities in high-temperature plasmas [1,2] is widely used in modeling of SOL plasma, plasma energy balance and “killer pellet” experiments [3-5]. Applicability of the steady-state, corona equilibrium model of the “average ion” for description of “killer pellet” experiments with fast transient phase has to be proved by means of both theoretical studies and experimental observations.

Tracer Encapsulated Solid PELlet (TESPEL) injection experiments in LHD which are described below give a good opportunity to check this applicability for different impurities since the tracer material could be varied. Besides, these experiments can

give new information about impurity pellet deposition and its correspondence to the pellet ablation rate profiles measured by pellet ablation light. A correspondence between pellet ablation and deposition was observed in impurity (Li, C) pellet injection experiments [6,7]. However, in hydrogen pellet experiments it was observed that the resulting distribution of electrons is better described by an assumption that the particles produced at a given point in the pellet ablation are spread more widely over the flux surfaces outboard of the ablation location [8,9].

In this paper, new experimental information on both problems mentioned above is presented.

Corresponding author's e-mail: sergeev@phf.stu.neva.ru

2. Apparatus and Experimental Results

TESPEL pellets are polystyrene (C_8H_8) balls of 0.70–0.85 mm diameter. It serves as a shell for a Ti tracer material (4–6 balls of about 0.1 mm diameter) that is put in the ball core [10]. In experiments, TESPEL was injected with $v_p = 0.35$ – 0.45 m/s velocities at the LHD equatorial plane from outboard side. Pellet ablation rate of both shell \dot{N}_{sh} and tracer material \dot{N}_{tr} was measured by means of total pellet cloud light at specific lines of shell H_α and tracer TiII using the light filters (656.3 ± 1.35 nm) and (400.3 ± 1 nm) correspondingly.

Absolute measurements of line-integrated total plasma radiation were performed by means of two arrays of AXUVD diodes which are situated in the same toroidal position above and below the equatorial plane with $\sim 8^\circ$ difference between viewing angles of the AXUVD pin-holes. The plasma cross-sections in the AXUVD and TESPEL toroidal positions have an elliptical shape ($\sim 0.8 \times 1.6$ m) elongated in the major radial direction. Arrays have 16 (AXUVD Upper array, $\bar{I}_U(t, y)$ signal) and 19 (AXUVD Lower array, $\bar{I}_L(t, y)$ signal) detectors so that their pin-holes provide about 5–7 cm distances between AXUVD channels in the vertical direction y . It allows us to make tomography reconstruction of the radiated power profile, $P_{rad}(\rho)$, versus effective plasma radius, ρ , prior to pellet injection.

Line integrated density evolutions $\bar{n}_e(t, R_{FIR})$ were measured using a 12 channel FIR laser interferometer [11]. FIR beams have ~ 4 cm width and pass through the plasma vertically where the plasma has a vertically elongated cross-section at fixed major radius positions R_{FIR} . Abel inversion of FIR data provided radial profile $N_{e0}(\rho)$ data prior the pellet injection.

Electron temperature profile data, $T_{e0}(\rho)$, prior pellet injection was measured by a multi (200) point TS technique [12]. The 16 channels super heterodyne receiver of $2\omega_{ce}$ harmonics provided temporal behavior of electron temperature $T_e(t, \rho_{ECE})$ at certain ρ_{ECE} radial positions [13].

Figures 1(a) and 1(b) shows temporal evolution of central line-integrated signals of electron density $\bar{n}_e(t, 0)$, upper $\bar{I}_U(t, 0)$ and lower $\bar{I}_L(t, 0)$ AXUVD arrays in case I of pure shell (a) and in case II of shell with Ti tracer (b) injections. Measured pellet ablation rates $\dot{N}_{par}(t)$ versus time are shown in particles per second units. Particles mean molecules for the shell material and Ti atoms for the tracer.

One can see from Fig. 1 that after pellet ablation starts at time t_0 , a fast transient occurs to a new quasi

steady-state of both electron density and plasma radiation established at time t_1 . Duration $t_1 - t_0$ differs for case I and II. This difference might be due to a presence of heavy Ti ions in case II leading to smaller values of ion-sonic speed $c_s \propto \sqrt{T_e/m_i}$ of ablatant flowing along magnetic field lines. Another reason is that the time needed for equilibrium ionization balance of Ti ions is longer than for carbon ones. As can be seen from Figs. 2(a) and 2(b) where radial $N_e(\rho)$, $T_e(\rho)$ profiles at times t_0 , t_1 are shown, T_e of 0.5–1 keV and N_e of $(3.5 - 4.5) \times 10^{13}$ cm $^{-3}$ after pellet injection were measured. According to calculations done in [14] by MIST code [15], one can conclude that for these T_e , N_e values at time t_1 a complete ionization of C occurs in case I and ionization up to either Be- or Li-like Ti ions dominates in case II. Times of subsequent ionization of Ti ions to

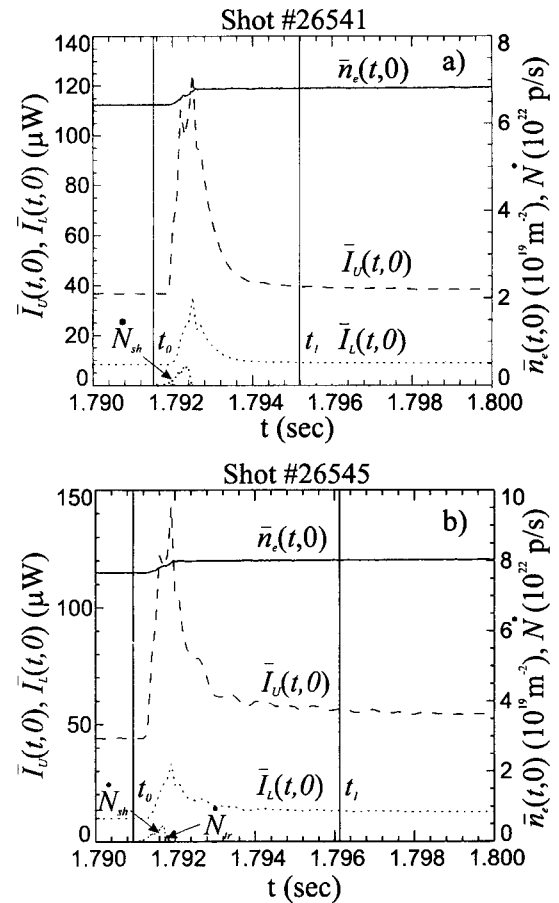


Fig. 1 Temporal evolution of central line-integrated signals of electron density, $\bar{n}_e(t, 0)$, upper $\bar{I}_U(t, 0)$ and lower $\bar{I}_L(t, 0)$ AXUVD arrays. Measured ablation rates of shell (dotted) and tracer (solid) are shown. Thin vertical lines depict times t_0 and t_1 ; a - case I; b - case II.

He- and H-like ionization states are much longer (50–80 ms) and comparable with the impurity transport time (see ref. [14]). Since the amount of tracer Ti particles (1.2×10^{17}) is much smaller than amount of shell particles ($\sim 1.55 \times 10^{18}$ C₈H₈ molecules for case I and 1.35×10^{18} for case II), the electron density increase should not be affected by detailed Ti ionization balance. On the contrary, radiation in case II is mainly determined by Ti ions as can be seen from Fig. 1 comparing the radiation increases in two cases at time t_1 . It is seen from Fig. 1 that after the establishment of ionization balance, a radiation perturbation due to a high Z Ti impurity is 3–5 times higher in case II than in case I.

3. Simulations and Discussion

We assumed that “average ion” model could be applied for times after t_1 and simulated the line-integrated density $\Delta \bar{n}_e(R_{\text{FIR}}) = \bar{n}_e(t_1, R_{\text{FIR}}) - \bar{n}_e(t_0, R_{\text{FIR}})$ and radiation $\Delta \bar{I}_{\text{U,L}}(y) = \bar{I}_{\text{U,L}}(t_1, y) - \bar{I}_{\text{U,L}}(t_0, y)$ increases between times t_1 and t_0 . Since we have localized perturbations due to pellet injection, simulation of line-integrated quantities was done to exclude additional uncertainties which usually occur applying the Abel inversion or tomography reconstruction for non-monotonic profiles.

For that, perturbed density profiles $N_{e1}(\rho) = N_{e0}(\rho) + \Delta N_{e1}(\rho)$ shown in Fig. 2 were calculated at time t_1 . The density increase just after pellet injection $\Delta N_e(\rho) = \Delta N_{\text{part}}(\rho) \langle Z(T_e(\rho)) \rangle$ was calculated using the measured particle deposition $\Delta N_{\text{part}}(\rho)$ profiles and $\langle Z(T_e) \rangle$ dependence of the “average ion” model. Assuming no drift of ablated material, the particle deposition profile was easily reconstructed from the pellet $\Delta N_{\text{part}}(\rho) = \dot{N}_{\text{part}}(\rho) dR/d\rho / (v_p dV/d\rho)$ ablation rate. Here, $dV/d\rho$ and $dR/d\rho$ are ρ derivative of plasma volume $V(\rho)$ and plasma major radius $R(\rho)$ along the pellet path (see details in ref. [6]).

Perturbation $\Delta T_e(\rho)$ of the electron temperature profile just after pellet injection was evaluated from the energy balance equation $N_e(\rho) T_e(\rho) = T_{e0}(\rho) N_{e0}(\rho) - 2/3 E_{\text{ion}}$ on the magnetic surface. Thus, adiabatic plasma cooling by cold ablatant electrons and energy losses E_{ion} for ionization of the ablatant were taken into account. Obtained $\Delta N_e(\rho)$, $\Delta N_{\text{part}}(\rho)$ and $\Delta T_e(\rho)$ profiles were diffused with 0.5 m²/s diffusion (heat conductivity) coefficient during $t_1 - t_0 = 3-5$ ms duration of transient time. It resulted in $\Delta N_{e1}(\rho)$, $\Delta N_{\text{part}1}(\rho)$ and $\Delta T_{e1}(\rho)$ radial profiles. Diffused profiles $N_{e1}(\rho) = N_{e0}(\rho) + \Delta N_{e1}(\rho)$ and $T_{e1}(\rho) = T_{e0}(\rho) + \Delta T_{e1}(\rho)$ are shown by thin solid lines in

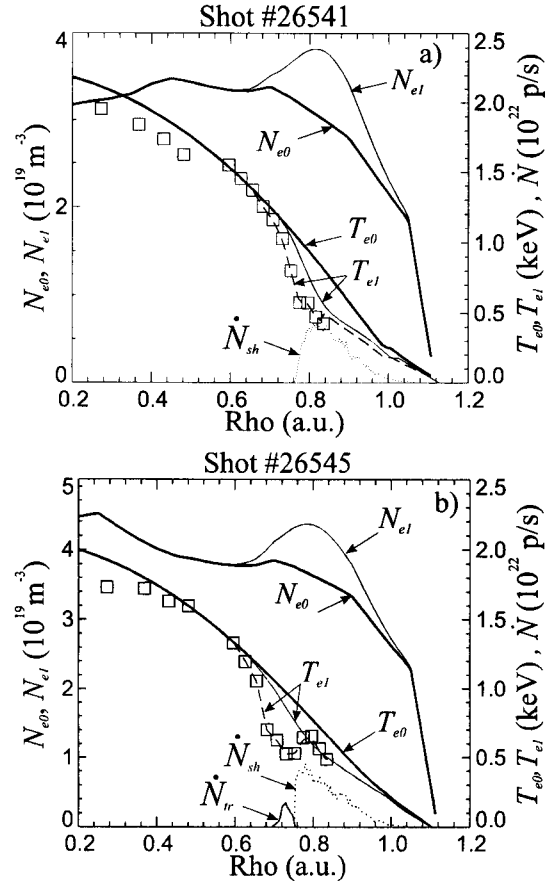


Fig. 2 Electron density and temperature profiles prior (thick) and after (thin) pellet injection. $N_{e0}(\rho)$, $T_{e0}(\rho)$ profiles are fit curves to experimental data. Measured ablation rate profiles of shell (dotted) and tracer (solid) are shown. Profile $T_e(t_1, \rho_{\text{ECE}})$ is shown by boxes: a - case I; b - case II.

Fig. 2. It is seen from Fig. 2 that these calculated $T_{e1}(\rho)$ values are slightly higher than the measured $T_e(\rho_{\text{ECE}}, t_1)$ shown by boxes in case I and essentially higher than one for case II. It might be due to additional electron energy losses of radiation which had not been taken into account in the energy balance equation solved.

For subsequent calculations of line-integrated $\Delta \bar{n}_e(R_{\text{FIR}})$ and $\Delta \bar{I}_{\text{U,L}}(y)$ signals, we constructed $T_{e1}(\rho)$ profiles using $T_e(\rho_{\text{ECE}}, t_1)$ profile up to its maximal effective radius and the $T_{e1}(\rho)$ simulated as described above. Evaluated $N_{e1}(\rho)$ (thin curve in Fig. 2) and created $T_{e1}(\rho)$ (dashed curves in Fig. 2) profiles were used for calculations of density and radiation perturbations. Diffused $\Delta N_{\text{part}1}(\rho)$ profiles of impurities injected were used with corresponding “average ion” model dependencies $\langle Q_{\text{rad}}(T_{e1}) \rangle$, $\langle Z(T_{e1}) \rangle$ for C and Ti

as well.

Results of comparison of measured and simulated increases of $\Delta\bar{n}_e(R_{\text{FIR}})$ and radiation $\Delta\bar{I}_{\text{U,L}}(y)$ are shown in Fig. 3 (case I) and Fig. 4 (case II) correspondingly. For calculations of the $\Delta\bar{I}_{\text{U,L}}(y)$ radiation increase we additionally took into account a perturbation of the intrinsic impurity radiation $P_{\text{intr1}}(\rho) = P_{\text{intr0}}(\rho)(1 + \Delta N_e(\rho)/N_{e0}(\rho))$. Because of unknown radial distributions of all intrinsic impurity species, we assumed here that $P_{\text{intr0}}(\rho)$ is determined by radiation of intrinsic impurities prior to pellet injection (neglecting the bremsstrahlung) and neglected a perturbation of T_e , i.e. assumed that a radiative rate $\langle Q_{\text{rad}}(T_{e1}) \rangle$ is unchanged for them.

One can see that this line-integrated $P_{\text{intr1}}(\rho)$ perturbation (dashed curves) is comparable with a perturbation caused by ablatant (dotted curves) in case I

(Figs. 3(b) and 3(c)) and it is significantly smaller than the one in case II (Figs. 4(b) and 4(c)) due to Ti tracer radiation. It is seen from Figs. 3 and 4, that both density and radiation increases due to pellet injection are rather well reproduced using “average ion” dependencies for both $\langle Z(T_e) \rangle$ and $\langle Q_{\text{rad}}(T_e) \rangle$. Some discrepancies of $\Delta\bar{I}_{\text{U,L}}(y)$ profiles may be connected with simplifications of modeling (for instance, a radiation perturbation of intrinsic impurities in case I etc.). The temperature 0.3–1 keV range of interest is seen from Fig. 2 as well. It means that the main impurity radiation should be in the VUV and SXR spectral regions, so that the lower sensitivity of the AXUVD detectors in the visible spectral range does not falsify our comparison.

Simulations have shown that calculated density and radiation increases are rather sensitive to the pellet

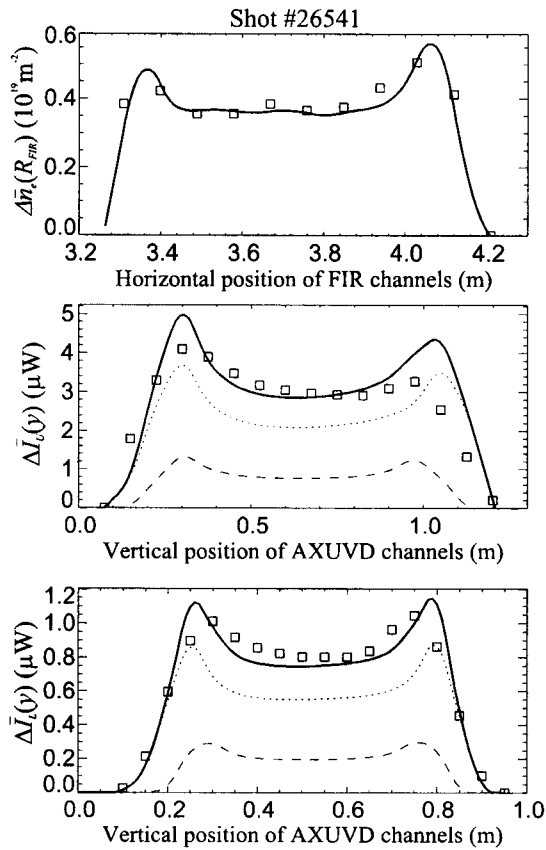


Fig. 3 Measured (boxes) and calculated (thick solid) perturbations of line-integrated electron density $\Delta\bar{n}_e(R_{\text{FIR}})$ and radiation $\Delta\bar{I}_{\text{U,L}}(y)$. Perturbations of $\Delta\bar{I}_{\text{U,L}}(y)$ signals due to TESPEL injection (dotted) and due to perturbation of intrinsic impurity radiation (dashed) are shown. Shell injection in shot #26541 (case I).

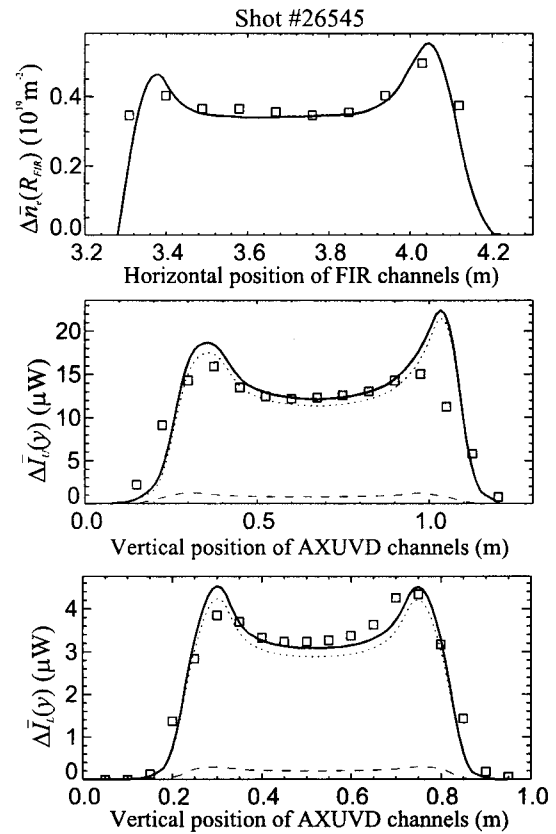


Fig. 4 Measured (boxes) and calculated (thick solid) perturbations of line-integrated electron density $\Delta\bar{n}_e(R_{\text{FIR}})$ and radiation $\Delta\bar{I}_{\text{U,L}}(y)$. Perturbations of $\Delta\bar{I}_{\text{U,L}}(y)$ signals due to TESPEL injection (dotted) and due to perturbation of intrinsic impurity radiation (dashed) are shown. Shell with Ti tracer injection in shot #26545 (case II).

deposition radial profile. Radial variations of pellet deposition profile with its ± 3 cm experimental accuracy can lead to well detected discrepancies of both $\Delta \bar{n}_e(R_{\text{FIR}})$ and $\Delta \bar{I}_{\text{U,L}}(y)$ profiles from those measured in experiment. This means that no significant drifts of ablatant affect the pellet deposition profiles in comparison with those evaluated using the pellet ablation light.

4. Conclusions

Perturbations of electron density and total plasma radiation profiles were measured and simulated in cases of both a pure polystyrene shell and shell with Ti tracer (TESPEL) pellet injections into LHD plasmas. After establishing ionization balance up to Li-like impurity ions of ablated material, a good agreement between measured and simulated profiles was obtained taking into account pellet deposition by ablation lights and using "average ion" dependencies on electron temperature for both impurity charge state $\langle Z(T_e) \rangle$ and radiative cooling rate $\langle Q_{\text{rad}}(T_e) \rangle$. One can conclude that the pellet deposition profile can be reasonably evaluated by the pellet ablation rate profile without significant drift influence on ablatant deposition. After establishing ionization balance, dependencies $\langle Q_{\text{rad}}(T_e) \rangle$, $\langle Z(T_e) \rangle$ are adequate in a 0.3–1 keV temperature range and a radiation increase in case II with high Z Ti impurity of the tracer material is 3–5 times higher than in case I of pure shell injection.

References

- [1] D.E. Post *et al.*, Atomic Data and Nuclear Data Tables **20**, 397 (1977).
- [2] R. Clark *et al.*, J. Nucl. Mater. **220-222**, 1016 (1995).
- [3] ITER Physics, Nucl. Fusion **39**, 2251 (1999).
- [4] S. Putvinski *et al.*, Plasma Phys. and Contrl. Fusion **39**, B157 (1997).
- [5] V.M. Timokhin *et al.*, Plasma Physics Rep. **27**, 1 (2001).
- [6] V. Yu. Sergeev *et al.*, Rev. Sci. Instrum **63**, 4984 (1992).
- [7] L. Ledl *et al.*, Europh. Conf. Abstr. **23J**, 1477 (1999).
- [8] L.R. Baylor *et al.*, Phys. Plasmas **7**, 1878 (2000).
- [9] R. Sakamoto *et al.*, Nucl. Fusion **41**, 3811 (2001).
- [10] K. Khlopenkov and S. Sudo, Plasma Phys. Contrl. Fusion **43**, 1547 (2001).
- [11] K. Kawahata *et al.*, Rev. Sci. Instrum **70**, 707 (1999).
- [12] K. Narihara *et al.*, Rev. Sci. Instrum **72**, 1122 (2001).
- [13] Y. Nagayama *et al.*, Rev. Sci. Instrum **70**, 1012 (1999).
- [14] V.Yu. Sergeev *et al.*, Plasma Phys. Contrl. Fusion **44**, 277 (2002).
- [15] R.A. Hulse, Nucl. Technol. **3**, 259 (1983).